Journal of Physics:
Condensed Matter

Plasmonic properties and stability of Au and Cu nanoparticles embedded in cerium oxide

To cite this article: Eleonora Spurio *et al* 2024 *J. Phys.: Condens. Matter* **36** 375003

OPEN ACCESS
IOP Publishing
Journal of Physics: Condensed Matter
J. Phys.: Condens. Matter **36** (2024) 375003 (9pp)
https://doi.org/10.1088/1361-648X/ad5633

Plasmonic properties and stability of Au and Cu nanoparticles embedded in cerium oxide

Eleonora Spurio[1,2,*], **Samuele Pelatti**[1,2], **Sergio D'Addato**[1,2] **and Paola Luches**[2]

[1] Dipartimento FIM, Università degli Studi di Modena e Reggio Emilia, Modena, Italy
[2] Istituto Nanoscienze, CNR (NANO-CNR), Modena, Italy

E-mail: eleonora.spurio@unimore.it

Received 7 December 2023, revised 14 March 2024
Accepted for publication 10 June 2024
Published 19 June 2024

Abstract

With the aim of sensitizing cerium oxide—a very important catalytic material—to visible light, its coupling with Au and Cu nanoparticles is investigated. The samples are grown by physical synthesis by embedding a layer of nanoparticles between two cerium oxide films. The films are controlled in composition by *in-situ* x-ray photoemission spectroscopy and in morphology by *ex-situ* scanning electron microscopy. The optical properties as a function of the oxide thickness, investigated by spectrophotometry in the UV-Vis range, are interpreted based on the results of the morphological characterization and of simulations based on the Maxwell Garnett model. The stability of chemical and optical properties after air exposure is also investigated. The results, indicating that stable materials with tuneable optical properties can be obtained, are important in view of the potential application of the investigated systems in photocatalysis.

Supplementary material for this article is available online

Keywords: metal nanoparticles, plasmonic properties, cerium oxide, optical properties

1. Introduction

Systems composed by plasmonic nanoparticles (NPs), such as Au, Ag and Cu, coupled with metal oxides (MOs) such as CeO_2 or TiO_2 are promising in the field of solar light photocatalysis [1–6], in which the photocatalytic properties of some MOs can be combined to the large absorption and scattering cross section in the visible range typical of plasmonic NPs [6]. The interaction of the incoming visible radiation with metallic NPs triggers localized surface plasmon resonances (LSPRs), collective oscillations of electrons at the surface of the nanostructures [5, 7–10]. The plasmonic properties strongly depend on the composition, size, shape and aspect ratio of the NPs and on the dielectric properties of the environment, that plays a relevant role in determining the polarizability and hence the optical response of the material. Moreover, when the NPs are surrounded by a semiconductor, the relaxation of the LSPRs in the metallic NPs may lead to a charge or energy transfer from the nanostructures to the semiconductor [3, 6, 11, 12]. The interaction between the plasmonic NPs and the surrounding material may involve different mechanisms, such as an increase of the length of the optical path due to light scattering or the transfer of charge and/or energy from the NPs to the semiconductor [5, 9, 12–14]. The efficiency of such processes is influenced by different factors, including the properties of the NPs, the dielectric properties of the environment, the quality of the interface between NPs and semiconductor and the band alignment of the two materials [5, 9, 14, 15]. The effect can be exploited to sensitize wide band gap oxides to visible light.

---

[*] Author to whom any correspondence should be addressed.

Cerium oxide is a semiconducting oxide with a band gap in the UV, between 3.2 and 4 eV depending on the defectivity [16–18]. It has relevant catalytic properties due to its reducibility that allows to easily and reversibly incorporate oxygen ions into its lattice [2, 4, 9, 12]. The possibility to enhance reducibility via coupling with plasmonic nanoparticles represents an appealing possibility to obtain more efficient catalysts.

In previous works by some of the authors, systems composed by Ag NPs coupled with CeO_2 have been systematically investigated in terms of morphology [19, 20], electronic and optical properties [21], and of dynamics of excited states [4, 8]. Ag is a strongly-plasmonic material predicted to have a very high hot electron generation rate [15], and Ag NPs have shown a highly efficient charge transfer upon the relaxation of LSPR excitations [3, 5, 7, 22, 23]. However, the material is also rather expensive, and Ag NPs undergo rapid corrosion in ambient air, altering their plasmonic properties [24, 25]. Au NPs, on the other hand, are inert in air, and they represent stable, though expensive, systems. Also Au NPs embedded within CeO_2 layers have shown a high plasmon-mediated charge transfer efficiency [26]. Cu, finally, is unstable in atmosphere, but it is less critical than Au and Ag, and its oxides also present interesting catalytic properties by themselves [27–29].

In the present work, samples composed by Au and Cu NPs embedded in CeO_2 matrices are investigated to study the influence of the environment and of the NP morphology on the optical properties of the systems. We demonstrate that systems composed by plasmonic NPs combined with CeO_2 present an intense light absorption in the visible range, that can be tuned by changing the dielectric or the NP properties. We also show that the optical properties of the investigated systems persist after a long period of air exposure, a very important requirement for the applications.

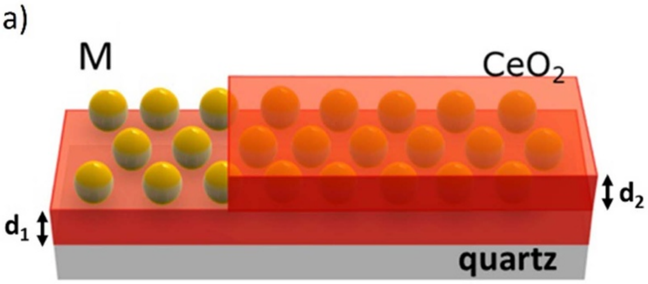

b)

Name	M	$d_1 = d_2$ (nm)
CeO_2	-	2
Bare Au	Au	0
Au@CeO_2 1.6 nm	Au	0.8
Au@CeO_2 4 nm	Au	2
Au@CeO_2 8 nm	Au	4
Bare Cu	Cu	0
Cu@CeO_2 1.6 nm	Cu	0.8
Cu@CeO_2 4 nm	Cu	2
Cu@CeO_2 8 nm	Cu	4

Figure 1. (a) Schematics of the sample used for the optical characterization: NPs embedded between two ceria layers of overall thickness $d_1 + d_2$; (b) table of the samples characterized in the present work.

2. Materials and methods

The samples here investigated are model systems composed of metal (Au or Cu NPs) embedded between two stoichiometric CeO_2 films of variable thickness. They were grown in the ultra-high vacuum (UHV) apparatus ($P \sim 10^{-10}$ mbar) described in [30], composed by two connected UHV chambers. The first one is equipped with evaporators and gas lines and it is used for sample deposition, while the second one is used for substrate preparation and electronic characterization through x-ray photoemission spectroscopy (XPS). Cerium oxide films were grown by reactive molecular beam epitaxy, evaporating Ce from an e-beam evaporator in an oxygen partial pressure of 10^{-7} mbar, while Cu and Au were deposited by Knudsen cells. The evaporators were calibrated using a quartz microbalance before the growth. The substrate was kept at room temperature (RT) during oxide and metal growth. The samples used for optical characterization (schematics in figure 1(a)) are composed by a layer of NPs embedded between two layers of CeO_2, grown on optical grade quartz substrates, transparent in the UV-Vis range. The layer of metal NPs was obtained by evaporating an equivalent thickness of 2 nm of metal, that nucleates into NPs when deposited on the oxide surface [1, 19, 20]. In all samples for optical characterization the NPs were embedded between two layers of ceria of the same thickness, that were varied between 0.8 and 4 nm as schematized in figure 1. Samples with bare NPs, deposited on quartz, and a CeO_2 film of 4 nm thickness were also used as references. The list of all samples is reported in figure 1(b). While the optical absorptance characterization requires a substrate that is transparent in the UV-Vis range, the SEM analysis must be performed on a conductive sample. Then, while the samples for the optical characterization have been grown on transparent quartz substrates, the samples for morphological characterization (schematics in figure S1) are composed by a 2 nm thick CeO_2 film with a layer of NPs (2 nm equivalent) on top, deposited on a Si substrate with a 600 nm thick thermal oxide film, that shows a high enough conductivity for scanning electron microscopy (SEM) analysis.

Both the quartz and the Si substrates were prepared by a 5 min bath in acetone at 423 K and by two subsequent ultrasonic baths in acetone and in isopropanol at 353 K for 3 min each. The sample morphology, and in particular the size, shape, and density of metal NPs are not expected to depend on the underlying ceria film thickness, nor on the substrate used, since the surface of CeO_2 films grown at room temperature has a granular rough morphology even on flat single crystal metal surfaces [30]. After the growth, all samples were characterized by in situ XPS using Al Kα photons from a double anode x-ray source, to obtain quantitative information on the deposited quantity of CeO_2 and metal and on possible variations of the chemical state of the materials composing the sample. SEM images of the samples were acquired using a FEI Nova Nano SEM450. The SEM column was equipped with a Schottky field-emission gun (SFEG), and it could achieve a resolution of 1.4 nm in a low-voltage (1 KV) operation. The GMS3 GATAN software by DigitalMicrograph and the ImageJ software developed by National Institutes of Health of United States were used to obtain the metal NPs size distribution.

The absorptance of the samples was analyzed through optical UV-Vis spectrophotometry. The setup is composed by a Xenon lamp that provides white non-polarized light, an ORIEL-MS257 monochromator, a polarizer and a silicon photodetector. The absorptance A of the sample is evaluated as $A = 1 - (T + R)$, where T and R are the transmittance and the reflectance, i.e. the fraction of transmitted and reflected light, measured with the impinging photon beam forming an angle of 22° with the sample surface normal. In this configuration, s polarization is entirely in the surface plane, while in the case of p polarization a small out-of-plane component is also present. For all samples, the shape of the spectra acquired with s- or p-polarized light is comparable (see supporting information figure S2), indicating that the samples are optically isotropic in the surface plane. The spectra shown in this work were all acquired with s-polarized radiation. The experimental results are compared with numerical calculations, obtained by performing polarizability simulations based upon the Maxwell Garnett model for optical absorption [31], using the AR obtained by the analysis of the SEM images (see supporting information for detail). For the simulations, the bulk dielectric functions were obtained from [32] for CeO_2 and from [33] for Au and Cu, while when simulating bare NPs on quartz, the real part of the complex refractive index for quartz was calculated from the Sellmeier equation [34] using the coefficient of fused silica (SiO_2) at RT [35].

3. Results and discussion

To analyze the NPs morphology, SEM images were acquired from samples composed of 2 nm CeO_2 + 2 nm M (M = Au, Cu). Representative images of the two samples, shown in figure 2, clearly show that Au forms smaller NPs than Cu on the CeO_2 surface. In both samples the NPs cover the whole sample surface with a constant density, suggesting that the CeO_2 film presents a uniform density of surface defects which possibly act as nucleation centers. Both Au and Cu NPs (figures 2(a) and (b) respectively) present an irregular shape, and the particles are partially interconnected. The lateral size distribution extracted from the SEM images (figures 2(a) and (b)), shows an average diameter of 6 nm for Au NPs, with a standard deviation of 3.4 nm, and of 15.1 nm for Cu NPs, with standard deviation of 10 nm. This value, in conjunction with a measure of the average NP thickness extracted from the fractional surface coverage, obtained from the SEM images, gives an estimation of the aspect ratio (AR) of the NPs, defined as the ratio between the *in-plane* and the *out-of-plane* size. The average AR is 2.2 for Au NPs and 5.3 for Cu NPs (see supporting information, figure S3, for more details and for the AR distribution). The AR of the NPs, together with their dielectric environment, are crucial aspects for the simulation of the optical properties of the samples [21, 36]. Comparing the average *out-of-plane* size of the NPs (∼2.7 nm and ∼3.3 nm for Cu and Au NPs respectively, see SI for more details) with the thickness of the uppermost ceria layer, the NPs result only partially covered by the ceria film, especially in the case of thin oxide layers.

The morphology of Au and Cu NPs on CeO_2 shows relevant differences. Au NPs appear smaller in size, with a lower AR, covering a smaller fraction of substrate as compared to the case of Cu NPs. The morphology of metal NPs on oxide surfaces indeed depends on the interaction between the deposited atoms and the substrate, although other factors, like substrate defectivity and growth temperature also play a role [37]. The initial stages of the nucleation of Au and Cu NPs on flat epitaxial CeO_2 films have been investigated using surface science techniques [38, 39]. Au, due to its electronic structure, interacts weakly with the substrate and it preferentially nucleates at step edges and at point defects on the terraces [39]. Cu instead shows a stronger interaction and it initially binds to the CeO_2 surface also via a transfer of electrons to Ce ions [38]. In the case here investigated—RT nucleation of Au and Cu on non-annealed, non-epitaxial cerium oxide films—the substrate morphology is far from ideal, with a high density of defects due to the preparation conditions chosen. The metal atoms are expected to initially nucleate at defect sites. As the growth proceeds, Au atoms tend to preferentially bind to Au sites, forming smaller NPs with a lower AR than Cu NPs, in which, on the contrary, the interaction between Cu and ceria favors larger in-plane sizes, higher AR and a larger surface coverage. In other words, as observed in the work by Plessow and Campbell, the lower the ratio between the adhesion energy (E_{edh}) and the free energy (γ), the closer will be the NP to a sphere than to a hemisphere [40]. The ratio E_{edh}/γ for metallic NPs deposited on cerium oxide depends on the stoichiometry of the film. By fitting the XPS Ce 3d lines in the samples containing both Au and Cu NPs in ceria, we extracted a dominant CeO_2 stoichiometry for the films: in this case, the E_{edh}/γ is around 0.84 for Au and 0.98 for Cu [37, 41, 42], justifying the shape of the deposited NPs.

Figure 3(a) shows the optical absorptance of Au and Cu NPs embedded in 4 nm of CeO_2 and of an oxide film of the same thickness without NPs for comparison. The cerium oxide film only shows a peak at 300 nm characteristic of band gap excitations in CeO_2 [16]. The combination with metal NPs introduces additional absorption features on the right side of the CeO_2-related feature, ascribed to interband transitions from the d-valence band to empty states in the s and p bands, expected to occur around 350 nm for Au NPs [43] and at 450 nm in Cu NPs [11]. Moreover, a broad absorptance band appears in the visible region, peaked around 700 nm for Au@CeO_2 and above 750 nm for Cu@CeO_2, ascribed to the excitation of LSPR in the NPs [8, 11]. The LSPR-related

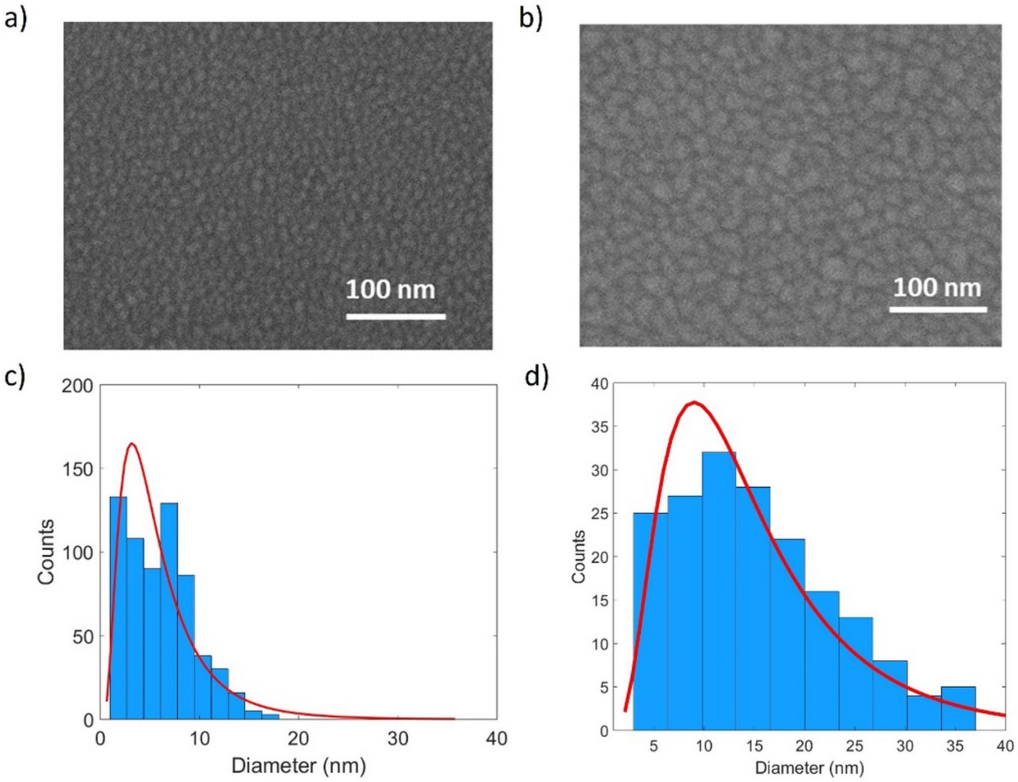

Figure 2. SEM images of (a) Au and (b) Cu NPs on CeO_2 films and corresponding diameter distribution (c) and (d), fitted with a lognormal function.

absorption band appears much broader for Cu NPs than for Au NPs. The optical absorptance intensity in the visible range is similar in the two samples with embedded NPs, meaning that all proposed materials have good plasmonic properties in the visible range, and that the plasmonic properties persist also after the short air exposure necessary to perform the optical measurements. This was expected for Au NPs, given the low reactivity of the material, while other works shown bare Cu NPs to undergo a progressive degradation of plasmonic properties after air exposure [44, 45], that depends on the size and shape of the NPs.

To understand the origin of the differences in the absorptance features in the visible range in Cu and Au NPs samples, the Maxwell Garnett model was used to simulate the polarizability of Au and Cu NPs embedded in CeO_2 (see supporting information for details) using the AR distribution obtained from the SEM images (figure 3(S), supporting information). For the simulations, the NPs were supposed to be immersed in a medium with the dielectric constant of bulk cerium oxide, to be non-interacting and to have an oblate spheroidal shape, since their average in-plane size is larger than their average height and they do not show any *in-plane* anisotropy. Figure 3(b) reports the imaginary part of the in-plane polarizability Im$\{\alpha_x\}$,proportional to the absorption cross section, simulated for both metals in CeO_2 for different values of AR (1, 1.5, 2 and 3). As shown in figure 3(b), spherical (AR = 1) Au NPs show a peak at 590 nm, very close in wavelength to the one observed for spherical Cu NPs. In both cases, an increase of the AR to values larger than 1 causes a red-shift of Im$\{\alpha_x\}$. Figure 3(c) presents the results of the simulations of the imaginary part of the *in-plane* polarizability Im$\{\alpha_x\}$ of Au/Cu NPs immersed in CeO_2 considering the AR distribution in figure S3 ranging from 1 to 4.5 for Au NPs and from 1 to 13 for Cu NPs and weighting each value for the weight of the corresponding AR in the distribution. The position and width of the absorptance features observed in figure 3(a) are qualitatively consistent with the behavior simulated in figures 3(b) and (c), with the Cu NP-related LSPR feature being broader and shifted towards higher wavelengths as compared to the case of Au NPs due to the broader AR distribution.

Figure 4(a) shows the static UV-Vis optical absorptance spectrum of bare Au NPs and of Au NPs embedded in ceria layers of different thicknesses. The bare Au NPs sample shows two broad bands, one extending from below 300 nm–490 nm, related to interband transitions, and a second one peaked around 610 nm, related to LSPR [8]. The addition of progressively thicker CeO_2 layers embedding the NPs introduces a CeO_2-related absorptance feature of increasing intensity and a gradual red-shift of the LSPR-related feature. A similar behavior was observed in similar systems composed of Au NPs surrounded by TiO_2 or Al_2O_3 [46]. The wavelength of the maximum absorptance of the plasmonic resonance peak is $\lambda_{\mathrm{bare}} = 603$ nm for bare Au NPs, it increases to $\lambda_{1.6} = 620$ nm when the NPs are immersed within a 1.6 nm ceria film, and it further shifts to $\lambda_4 = 645$ and finally to $\lambda_8 = 690$ nm for ceria layer thicknesses of 4 nm and 8 nm respectively. Also in this case, the changes observed in the

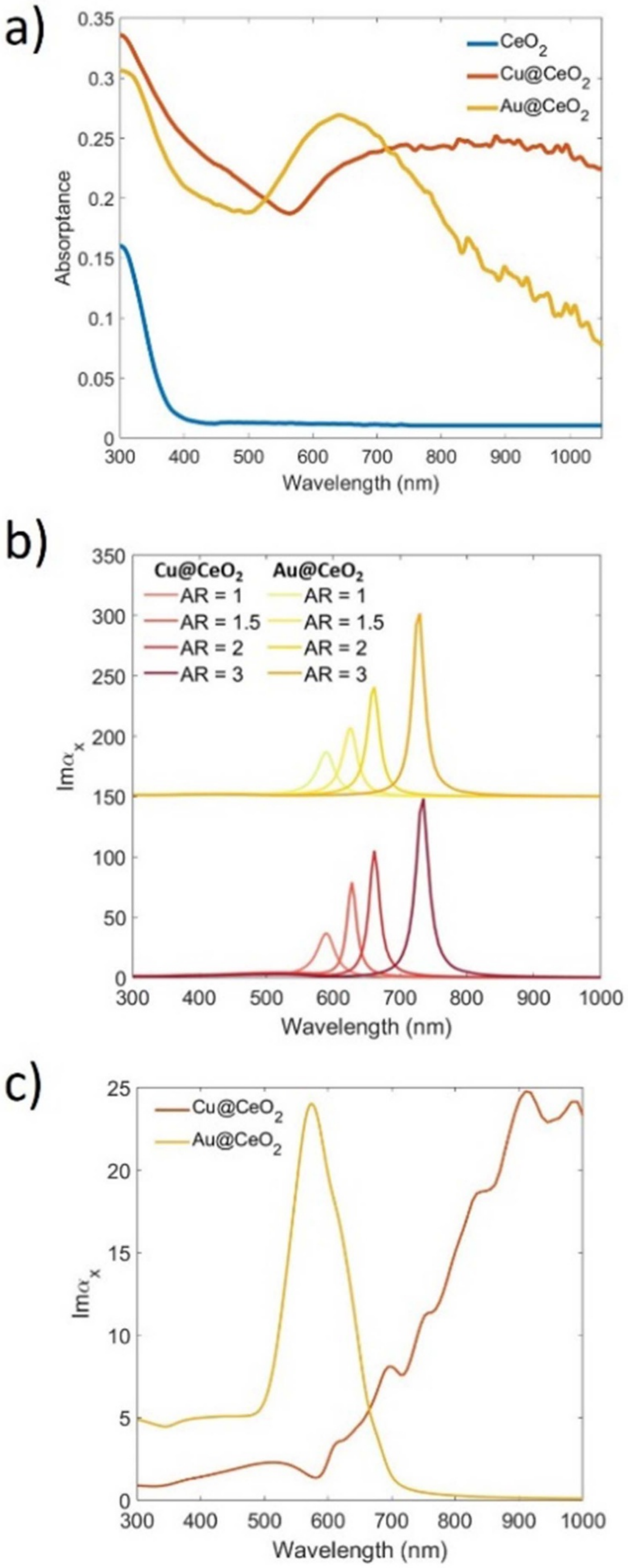

Figure 3. (a) UV-Vis absorptance spectra of Au and Cu NPs embedded in 4 nm CeO_2 and of a 4 nm CeO_2 film; (b) simulated imaginary part of the in-plane polarizability of Au and Cu NPs of different AR embedded within CeO_2; (c) simulated imaginary part of the in-plane polarizability of Au and Cu NPs with AR distribution extracted from the SEM images.

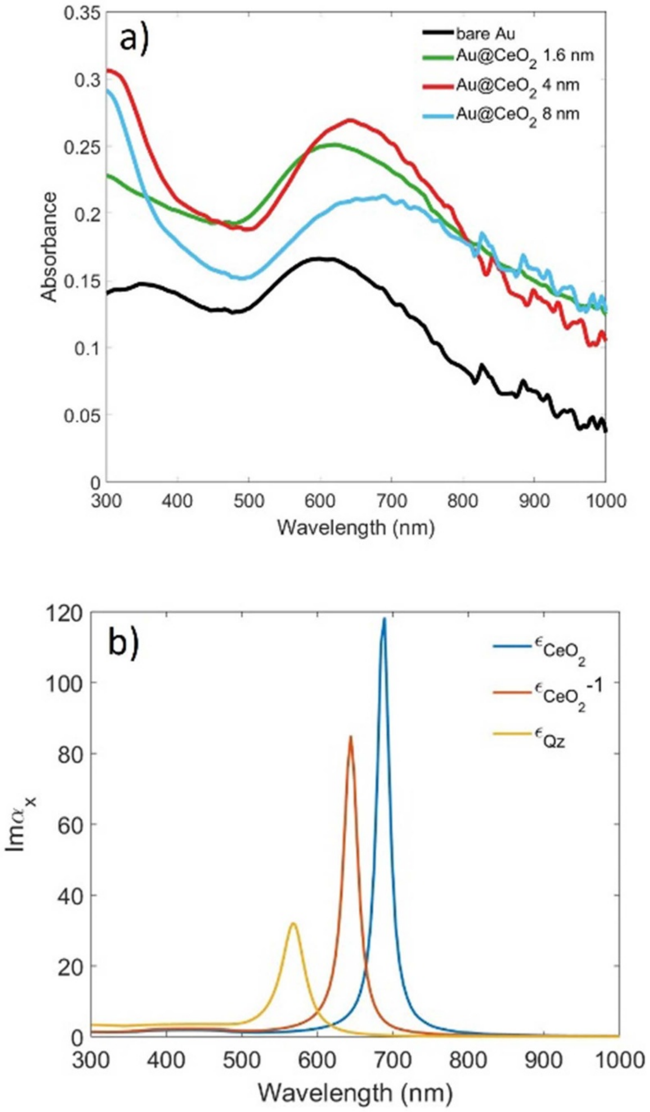

Figure 4. (a) UV-Vis absorptance spectra of Au NPs deposited on quartz embedded within CeO_2 films of different thickness; (b) simulated imaginary part of the in-plane polarizability of Au NPs with AR = 2.2 embedded within media with different dielectric functions.

optical properties are interpreted based on the results of the simulations of the imaginary part of the in-plane polarizability, reported in figure 4(b), for Au NPs with $\langle AR \rangle = 2.2$ (average AR obtained from the SEM images) surrounded by different dielectric environments. To simulate the optical properties of bare Au NPs on the quartz substrate, the NPs have been assumed for simplicity to be completely immersed in a quartz matrix. Furthermore, to account for the finite thickness of the ceria layer, the polarizability of NPs in a ceria layer with a smaller dielectric function (i.e. $\varepsilon_{CeO2} - 1$) was also simulated, as done in [21, 33, 47].

Expectedly, in figure 4(b) an increase of the dielectric function causes a red-shift of the peak wavelength, in agreement also with previous observations on Ag NPs [21]. The general trend observed experimentally for the LSPR band position as a function of the ceria layer thickness is therefore consistent with the results of the simulations. Indeed, the experimental LSPR band is much broader than the simulations, because it includes the contributions of all NPs, characterized by a wide distribution of ARs, while in this case only the average AR is considered for the simulation. The increase of the ceria layer thickness causes an increase in the absorptance intensity, reaching a maximum at 4 nm, and decreasing in the case of 8 nm.

The observed increase in absorptance with increasing ceria thickness is coherent with the increase of intensity of $\mathrm{Im}\{\alpha_x\}$ with increasing dielectric function in the calculations shown in figure 4(b). On the contrary, the decrease in absorptance intensity when the overall ceria layer is increased to 8 nm was less expected, and it is tentatively ascribed to some variation of the interparticle interaction that are not considered in the model. Both the optical spectrum and the Au 4f XPS line were almost unmodified 3 months after sample deposition (see supporting information, figure S4), demonstrating a good stability of the plasmonic properties of such material.

Figure 5(a) shows the optical absorptance spectrum of a layer of Cu NPs either bare or surrounded by two ceria layers of different thicknesses (1.6, 4 and 8 nm). The bare Cu NPs sample shows two broad bands, one extending from 300 nm to 550 nm, related to interband transitions, and a second one peaked around 750 nm, related to LSPR [11, 27]. The absorptance of the system composed by Cu NPs and CeO_2 shows an additional peak in the UV range, corresponding to band gap excitation of ceria. The wavelength of the LSPR band maximum of the different samples are $\lambda_{\mathrm{bare}} = 744$ nm, $\lambda_{1.6} = 810$ nm, $\lambda_4 = 890$ nm and $\lambda_8 = 1000$ nm. The behavior of the plasmonic resonance maximum with respect to the oxide thickness is in agreement with the behavior predicted by the simulations in figure 5(b), that reports the simulated imaginary part of the in-plane polarizability of Cu NPs with $<\mathrm{AR}> = 5.3$ (i.e. the average AR obtained from the SEM images). The simulations show a red-shift of the peak wavelength with increasing dielectric function, in analogy with the case of Au NPs. The same considerations concerning the width of the experimental LSPR-related band done for Au NPs also apply to Cu NPs.

For this sample, the intensity of the LSPR peak is maximum when the NPs are surrounded by an oxide layer of 1.6 nm thickness, and it decreases for thicker layers, remaining almost stable in the case of 4 nm or 8 nm of ceria. Also in this case, the trend, contrasting with the theoretical predictions, can be possibly ascribed to differences in the interparticle interactions with increasing ceria layer thickness.

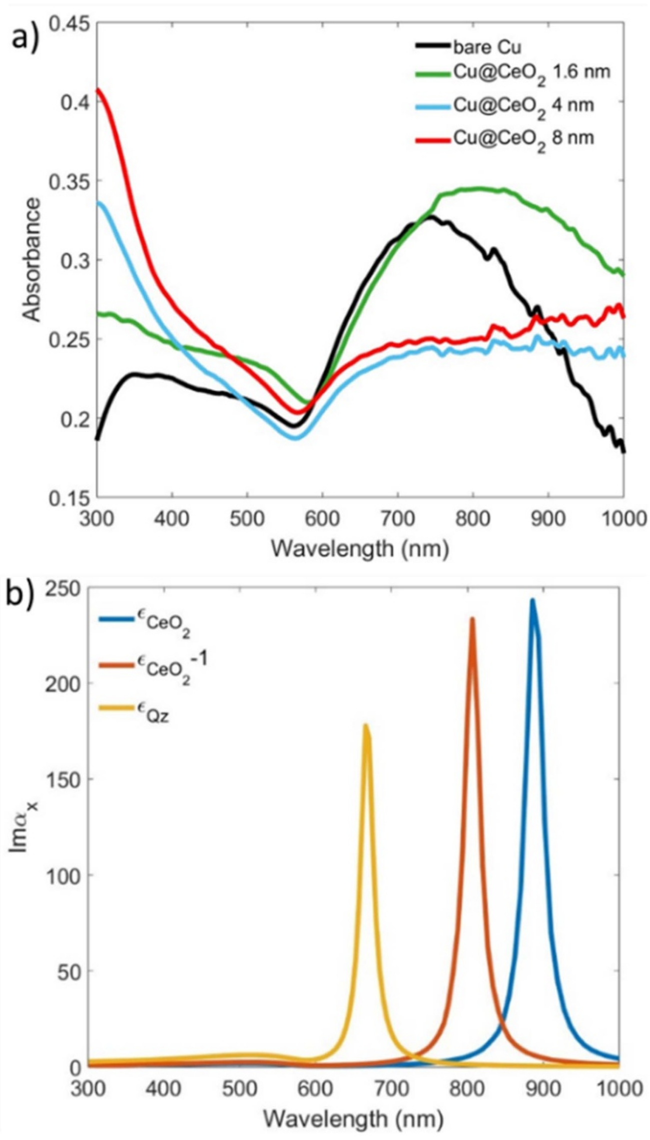

Figure 5. (a): UV-Vis absorptance spectra of Cu NPs embedded within CeO_2 films of different thickness; (b) simulated imaginary part of the in-plane polarizability of Cu NPs with the average AR = 5.3 embedded within media of different dielectric functions.

As for the Au NPs, also the stability of the plasmonic properties of the Cu NPs has been evaluated by repeating the optical and Cu 2p XPS measurements after 3 months from the deposition of the system, kept in a controlled N_2 atmosphere, at RT and with O_2 and humidity levels below a few ppm. Figure 6(a) shows the optical absorptance spectra of the bare Cu NPs as-grown and 3 months after the deposition, together with the optical absorptance of Cu NPs surrounded by a CeO_2 film of 4 nm. The plasmonic resonance band of the bare Cu NPs sample after three months is less intense, broader and red-shifted, consistently with the formation of a native oxide shell [45, 48]. On the other hand, the absorptance spectrum remains almost unmodified when the Cu NPs are embedded in 4 nm of cerium oxide, suggesting that the NPs are protected from oxidation by the cerium oxide layer in the considered time window, and that the plasmonic properties of the NPs remain essentially unmodified. To have a better understanding of the modifications induced by air on the surface of the bare Cu NPs, XPS and Auger Emission Spectroscopy (AES) measurements were performed on the bare Cu NPs sample as-grown and after 3 months from the growth. The Cu 2p spectrum in figure 6(b) provides information on the chemical state of the NP surface. The sample measured as-grown, i.e. before air

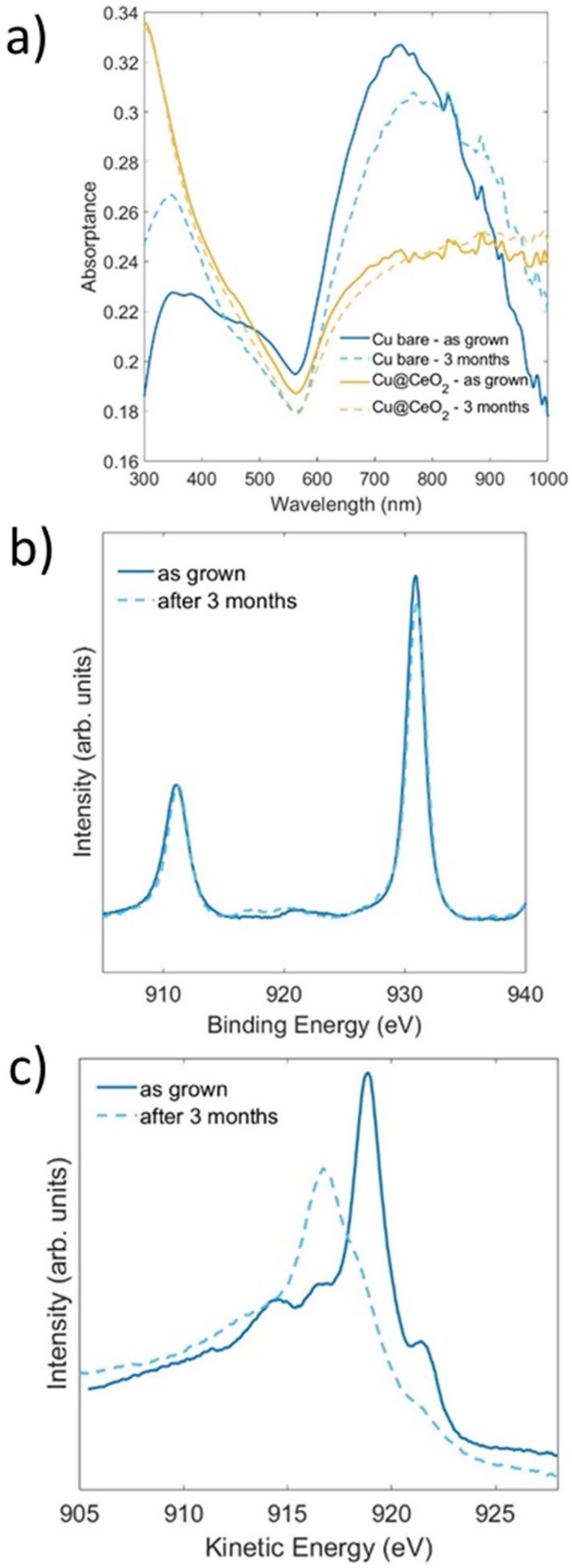

Figure 6. (a) Optical absorptance of the sample composed by bare NPs and Cu NPs embedded within 4 nm of CeO_2 after growth and after 3 months in controlled N_2 atmosphere. (b) Cu 2p XPS and (c) Cu LMM AES lines of the sample composed by bare Cu NPs after the growth and after 3 months.

exposure, exhibits the Cu 2p line-shape typical of metallic Cu, with well separated peaks corresponding to Cu $2p_{1/2}$ and Cu $2p_{3/2}$ [49]. The Cu 2p lines measured 3 months after the growth show a mild increase of the relative intensity of the shake-up satellite peaks between the Cu $2p_{1/2}$ and Cu $2p_{3/2}$ lines, typical of the Cu(II) and the Cu(I) species, suggesting an increase in copper oxide concentration [50, 51]. To have a clearer indication of the oxidation state of the NPs, the Cu L_3MM AES lines were also measured (figure 6(c)), being more sensitive to the oxidation state of Cu with respect to XPS [49, 52, 53]. The sample measured as-grown, i.e. before air exposure, exhibits the typical line-shape of metallic Cu, with the main peak at 918.6 eV [52], while after 3 months the sample presents a dominant peak at 916.8 eV, characteristic of cuprous oxide [52], coherently with a partial and superficial oxidation of the bare Cu NPs.

4. Conclusions

Composite systems made of Au and Cu NPs evaporated by molecular beam epitaxy embedded within cerium oxide films of different thicknesses show a strong and broad LSPR-related absorptance in the visible range. Au nucleates into smaller and more uniform NPs on the CeO_2 surface that give rise to a sharper LSPR-related absorptance band peaked at lower wavelengths as compared to the one shown by Cu NPs. The optical absorptance band of Au NPs can be shifted between approximately 600 nm and 700 nm by changing the thickness of the cerium oxide matrix. In the case of Cu NPs the shift is more significant, ranging from approximately 750 nm to above 1000 nm, due to the AR distribution of Cu NPs that is broader and shifted to higher values as compared to the one observed for Au NPs. The systems were shown to be stable for 3 months in controlled N_2 conditions. The stability is particularly significant in the case of Cu NPs, that tend to be oxidized by air exposure, while, if embedded within cerium oxide protective layers, they keep their plasmonic properties for relatively long times. The results represent a basis for the development of sustainable materials with high visible light conversion efficiency.

Data availability statement

All data that support the findings of this study are included within the article (and any supplementary files).

Acknowledgments

This work was supported by the PNRR MUR project ECS_00000033_ECOSISTER and by the European Union - NextGenerationEU (National Sustainable Mobility Center CN00000023, Italian Ministry of University and Research Decree no. 1033, 17/06/2022, Spoke 11, Innovative Materials & Lightweighting).

ORCID iDs

Eleonora Spurio https://orcid.org/0000-0002-0708-0299
Sergio D'Addato https://orcid.org/0000-0002-2002-2069
Paola Luches https://orcid.org/0000-0003-1310-5357

References

[1] Tian Y and Tatsuma T 2005 Mechanisms and applications of plasmon-induced charge separation at TiO_2 films loaded with gold nanoparticles *J. Am. Chem. Soc.* **127** 7632–7

[2] Primo A, Marino T, Corma A, Molinari R and García H 2011 Efficient visible-light photocatalytic water splitting by minute amounts of gold supported on nanoparticulate CeO_2 obtained by a biopolymer templating method *J. Am. Chem. Soc.* **133** 6930–3

[3] Pelli Cresi J S *et al* 2019 Highly efficient plasmon-mediated electron injection into cerium oxide from embedded silver nanoparticles *Nanoscale* **11** 10282–91

[4] Kim S M, Lee H, Goddeti K C, Kim S H and Park J Y 2015 Photon-induced hot electron effect on the catalytic activity of ceria-supported gold nanoparticles *J. Phys. Chem.* C **119** 16020–5

[5] Wu N 2018 Plasmonic metal–semiconductor photocatalysts and photoelectrochemical cells: a review *Nanoscale* **10** 2679–96

[6] Li B, Gu T, Ming T, Wang J, Wang P, Wang J and Yu J C 2014 (Gold core)@(ceria shell) nanostructures for plasmon-enhanced catalytic reactions under visible light *ACS Nano* **8** 8152–62

[7] Pelli Cresi J P *et al* 2021 Ultrafast dynamics of plasmon-mediated charge transfer in Ag@CeO_2 studied by free electron laser time-resolved x-ray absorption spectroscopy *Nano Lett.* **21** 1729–34

[8] Ratchford D C, Dunkelberger A D, Vurgaftman I, Owrutsky J C and Pehrsson P E 2017 Quantification of efficient plasmonic hot-electron injection in gold nanoparticle–TiO_2 films *Nano Lett.* **17** 6047–55

[9] Zhang Y, He S, Guo W, Hu Y, Huang J, Mulcahy J R and Wei W D 2018 Surface-plasmon-driven hot electron photochemistry *Chem. Rev.* **118** 2927–54

[10] Liu Z, Hou W, Pavaskar P, Aykol M and Cronin S B 2011 Plasmon resonant enhancement of photocatalytic water splitting under visible illumination *Nano Lett.* **11** 1111–6

[11] Lee C, Parkbc Y and Park J Y 2019 Hot electrons generated by intraband and interband transition detected using a plasmonic Cu/TiO_2 nanodiode *RSC Adv.* **9** 18371–6

[12] Wu K, Chen J, Mcbride J R and Lian T 2015 Efficient hot-electron transfer by a plasmon-induced interfacial charge-transfer transition *Science* **349** 632–5

[13] Navalon S, de Miguel M, Martin R, Alvaro M and Garcia H 2011 Enhancement of the catalytic activity of supported gold nanoparticles for the Fenton reaction by light *J. Am. Chem. Soc.* **133** 2218–26

[14] Atwater H and Polman A 2010 Plasmonics for improved photovoltaic devices *Nat. Mater.* **9** 205–13

[15] Liu T, Besteiro L V, Wanga Z and Govorov A O 2019 Generation of hot electrons in nanostructures incorporating conventional and unconventional plasmonic materials *Faraday Discuss.* **214** 199–213

[16] Pelli Cresi J S, Di Mario L, Catone D, Martelli F, Paladini A, Turchini S, D'Addato S, Luches P and O'Keeffe P 2020 Ultrafast formation of small polarons and the optical gap in CeO_2 *J. Phys. Chem. Lett.* **11** 5686–91

[17] Guo S, Arwin H, Jacobsen S N, Järrendahl K and Helmersson U 1995 A spectroscopic ellipsometry study of cerium dioxide thin films grown on sapphire by rf magnetron sputtering *J. Appl. Phys.* **77** 5369–76

[18] Patsalas P, Logothetidis S, Sygellou L and Kennou S 2003 Structure-dependent electronic properties of nanocrystalline cerium oxide films *Phys. Rev.* B **68** 035104

[19] Benedetti F, Luches P, Spadaro M C, Gasperi G, D'Addato S, Valeri S and Boscherini F 2015 Structure and morphology of silver nanoparticles on the (111) surface of cerium oxide *J. Phys. Chem.* C **119** 6024

[20] Luches P, Pagliuca F, Valeri S, Illas F, Preda G and Pacchioni G 2012 Nature of Ag islands and nanoparticles on the CeO_2(111) surface *J. Phys. Chem.* C **116** 1122–32

[21] Pelli Cresi J S, Silvagni E, Bertoni G, Spadaro M C, Benedetti S, Valeri S, D'Addato S and Luches P 2020 Optical and electronic properties of silver nanoparticles embedded in cerium oxide *J. Chem. Phys.* **152** 114704

[22] Pelli Cresi J S *et al* 2022 Lifetime of photogenerated positive charges in hybrid cerium oxide-based materials from space and mirror charge effects in time-resolved photoemission spectroscopy *J. Phys. Chem.* C **126** 11174–81

[23] Awazu K, Fujimaki M, Rockstuhl C, Tominaga J, Murakami H, Ohki Y, Yoshida N and Watanabe T 2008 A plasmonic photocatalyst consisting of silver nanoparticles embedded in titanium dioxide *J. Am. Chem. Soc.* **130** 1676–80

[24] Keast V J 2022 Corrosion processes of silver nanoparticles *Appl. Nanosci.* **12** 1859–68

[25] Mcmahon M D, Lopez R, Meyer H M, Feldman L C and Haglund R F 2005 Rapid tarnishing of silver nanoparticles in ambient laboratory air *Appl. Phys.* B **80** 915–21

[26] Spurio E, Pelli Cresi J S, Ammirati G, Pelatti S, Paladini A, D'Addato S, Turchini S, O'Keeffe P, Catone D and Luches P 2023 Injecting electrons into CeO_2 via photoexcitation of embedded Au nanoparticles *ACS Photonics* **10** 1566–74

[27] Dabera G, Walker M, Sanchez A M, Pereira H J, Beanland R and Hatton R A 2017 Retarding oxidation of copper nanoparticles without electrical isolation and the size dependence of work function *Nat. Commun.* **8** 1894

[28] Ghadimkhani G, de Tacconi N R, Chanmanee W, Janaky C and Rajeshwar K 2013 Efficient solar photoelectrosynthesis of methanol from carbon dioxide using hybrid CuO-Cu_2O semiconductor nanorod arrays *Chem. Commun.* **49** 1297–9

[29] Anandan S, Wen X and Yang S 2005 Room temperature growth of CuO nanorod arrays on copper and their application as a cathode in dye-sensitized solar cells *Mater. Chem. Phys.* **93** 35–40

[30] Luches P, Pagliuca F and Valeri S 2011 Morphology, stoichiometry, and interface structure of CeO_2 ultrathin films on Pt(111) *J. Phys. Chem.* C **115** 10718–26

[31] Granqvist C G and Hunderi O 1977 Optical properties of ultrafine gold particles *Phys. Rev.* B **16** 3513

[32] Fu-Chien C and Chih-Ming L 2010 Optical and electrical characterizations of cerium oxide thin films *J. Phys. D: Appl. Phys.* **43** 075104

[33] McPeak K M, Jayanti S V, Kress S J P, Meyer S, Iotti S, Rossinelli A and Norris D J 2015 Plasmonic films can easily be better: rules and recipes *ACS Photonics* **2** 326–33

[34] Ghosh G 1997 Sellmeier coefficients and dispersion of thermo-optic coefficients for some optical glasses *Appl. Opt.* **36** 1540–6

[35] Ghosh G, Endo M and Iwasaki T 1994 Temperature-dependent Sellmeier coefficients and chromatic dispersions for some optical fiber glasses *J. Lightwave Technol.* **12** 1338–42

[36] Simonsen I, Lazzari R, Jupille J and Roux S 2000 Numerical modeling of the optical response of supported metallic particles *Phys. Rev.* B **61** 7722

[37] Campbell T 1997 Ultrathin metal films and particles on oxide surfaces: structural, electronic and chemisorptive properties *Surf. Sci. Rep.* **27** 1–111

[38] Li G, Hu S, Xu Q and Zhu J 2019 Interaction between Cu nanoparticles and CeO_2(111) film surfaces *J. Phys. Chem.* C **123** 23563–71

[39] Lu J L, Gao H J, Shaikhutdinov S and Freund H J 2007 Gold supported on well-ordered ceria films: nucleation, growth and morphology in CO oxidation reaction *Catal. Lett.* **114** 8–16

[40] Plessow P and Campbell C T 2022 Influence of adhesion on the chemical potential of supported nanoparticles as modeled with spherical caps *ACS Catal.* **12** 2302–8

[41] Hemmingson S L and Campbell C T 2017 Support effects in catalysis and nanotechnology *ACS Nano* **11** 1196–203

[42] Hemmingson S L, James T E, Feeley G M, Tilson A M and Campbell C T 2016 Adsorption and adhesion of Au on reduced $CeO_2(111)$ surfaces at 300 and 100 K *J. Phys. Chem.* C **120** 12113–24

[43] Balamurugan B and Maruyama T 2005 Evidence of an enhanced interband absorption in Au nanoparticles: size-dependent electronic structure and optical properties *Appl. Phys. Lett.* **87** 143105

[44] Chan G H, Zhao J, Hicks E M, Schatz G C and Van Duyne R P 2007 Plasmonic properties of copper nanoparticles fabricated by nanosphere lithography *Nano Lett.* **7** 1947–52

[45] Susman M D, Vaskevich A and Rubinstein I 2016 A general kinetic-optical model for solid-state reactions involving the nano Kirkendall effect. The case of copper nanoparticle oxidation *J. Phys. Chem.* C **120** 16140–52

[46] Weng Y, Chen G, Zhou X, Zhang Y, Yan Q and Guo T 2022 Photoluminescence enhancement of quantum dots with different emission wavelengths using oxide shell-isolated Au nanoparticles *J. Mater. Sci.* **57** 7642–52

[47] Pascua L, Stavale F, Nilius N and Freund H 2016 Ag/ZnO hybrid systems studied with scanning tunnelling microscopy-based luminescence spectroscopy *J. Appl. Phys.* **119** 095310

[48] Rice K P, Walker E J, Stoykovich M P and Saunders A E 2011 Solvent-dependent surface plasmon response and oxidation of copper nanocrystals *J. Phys. Chem.* C **115** 1793–9

[49] Poulston S, Parlett P M, Stone P and Bowker M 1996 Surface oxidation and reduction of CuO and Cu_2O studied using XPS and XAES *Surf. Interface Anal.* **24** 811–20

[50] Pauly N, Tougaard S and Yubero F 2014 Determination of the Cu 2p primary excitation spectra for Cu, Cu_2O and CuO *Surf. Sci.* **620** 17–22

[51] Schön G 1973 ESCA studies of Cu, Cu_2O and CuO *Surf. Sci.* **35** 96–108

[52] Biesinger M C 2017 Advanced analysis of copper x-ray photoelectron spectra *Surf. Interface Anal.* **49** 1325–34

[53] Gloystein A and Nilius N 2020 High-pressure oxidation of copper on Au(111)—a route toward bulk-like cuprous oxide films *J. Phys. Chem.* C **124** 28605–13